

See discussions, stats, and author profiles for this publication at: <https://www.researchgate.net/publication/26333563>

ChemInform Abstract: X-Ray Diffraction, X-Ray Photoelectron Spectra, Crystal Structure, and Optically Properties of Centrosymmetric Strontium Borate Sr₂B₁₆O₂₆

ARTICLE *in* THE JOURNAL OF PHYSICAL CHEMISTRY B · AUGUST 2009

Impact Factor: 3.3 · DOI: 10.1021/jp903170p · Source: PubMed

CITATIONS

6

READS

63

4 AUTHORS, INCLUDING:



[Ali H Reshak](#)

University of West Bohemia

477 PUBLICATIONS 3,402 CITATIONS

[SEE PROFILE](#)



[Sushil Auluck](#)

Indian Institute of Technology Kanpur

313 PUBLICATIONS 3,084 CITATIONS

[SEE PROFILE](#)



[Iwan V Kityk](#)

Czestochowa University of Technology

959 PUBLICATIONS 7,933 CITATIONS

[SEE PROFILE](#)

X-ray Diffraction, X-ray Photoelectron Spectra, Crystal Structure, and Optical Properties of Centrosymmetric Strontium Borate $\text{Sr}_2\text{B}_{16}\text{O}_{26}$

Ali Hussain Reshak,^{*†} S. Auluck,[‡] I. V. Kityk,[§] and Xuean Chen^{||}

Institute of Physical Biology, South Bohemia University, Nove Hrady 37333, Czech Republic, Physics Department, Indian Institute of Technology Kanpur, Kanpur (UP) 208016, India, Electrical Engineering Department, Technological University of Czestochowa, Al Armii Krajowej 17/19, Czestochowa, Poland, and College of Materials Science and Engineering, Beijing University of Technology, Ping Le Yuan 100, Beijing 100124, People's Republic of China

Received: April 6, 2009; Revised Manuscript Received: May 12, 2009

We report results of X-ray diffraction (XRD) and valence band X-ray photoelectron (VB-XPS) spectra for strontium borate $\text{Sr}_2\text{B}_{16}\text{O}_{26}$. The X-ray structural analysis shows that the single crystals of $\text{Sr}_2\text{B}_{16}\text{O}_{26}$ crystallize in the monoclinic space group $P2_1/c$ with $a = 8.408(1)$ Å, $b = 16.672(1)$ Å, $c = 13.901(2)$ Å, $\beta = 106.33(1)$ °, and $Z = 4$. The crystal structure consists of a 3D network of the complex borate anion $[\text{B}_{16}\text{O}_{20}\text{O}_{12}]^{4-}$, formed by 12 BO_3 triangles and four BO_4 tetrahedra, which can be viewed as three linked $[\text{B}_3\text{O}_3\text{O}_{4/2}]^-$ triborate groups bonded to one pentaborate $[\text{B}_5\text{O}_6\text{O}_{4/2}]^-$ group and two BO_3 triangles. Using this structure, we have performed theoretical calculations using the all-electron full potential linearized augmented plane wave (FP-LAPW) method for the band structure, density of states, electron charge density, and the frequency-dependent optical properties. Our experimental VB-XPS of $\text{Sr}_2\text{B}_{16}\text{O}_{26}$ is compared with results of our FP-LAPW calculations. Our calculations show that the valence band maximum (VBM) and conduction band minimum (CBM) are located at Γ of the Brillouin zone (BZ) resulting in a direct energy gap of about 5.31 eV. Our measured VB-XPS show reasonable agreement with our calculated total density of states for the valence band that is attributed to the use of the full potential method.

1. Introduction

Borates are among the most interesting and therefore the most extensively studied materials. Since 1962, when the binary phase diagram $\text{Bi}_2\text{O}_3-\text{B}_2\text{O}_3$ was investigated, many methods for growth of the borate crystals were designed and described in detail in the literature.^{1–6} Theoretical exploration has shown that anionic groups and chemical bonding structures and coordination of boron atoms have a principal influence on the nonlinear optical properties of these crystals.^{7,8} Borate materials are of considerable interest because they show a great variety of physical properties ranging from nonlinear optical (NLO), ferroelectric to semiconducting behaviors, and in addition, a boron atom may adopt triangular or tetrahedral oxygen coordination, the BO_3 and BO_4 groups may be further linked via common oxygen atoms to form isolated rings and cages or polymerize into infinite chains, sheets, and networks, leading to the rich structural chemistry.^{9,10}

With a view of finding new optical materials, the alkaline earth metal borates have been extensively studied because $\beta\text{-BaB}_2\text{O}_4$ is an excellent NLO crystal primarily used in laser frequency conversion¹¹ and SrB_4O_7 was shown to be a potential NLO material with excellent mechanical and optical properties including a high second harmonic generation (SHG) coefficient, high optical damage threshold, and high hardness, etc.¹² In the system of $\text{SrO}-\text{B}_2\text{O}_3$, four phases with $\text{B}_2\text{O}_3/\text{SrO}$ ratios of 0.33–2.0 have been structurally characterized, which are

$\text{Sr}_3\text{B}_2\text{O}_6$,¹³ $\text{Sr}_2\text{B}_2\text{O}_5$,¹⁴ SrB_2O_4 ,^{15,16} and SrB_4O_7 .¹⁷ Among them, $\text{Sr}_3\text{B}_2\text{O}_6$ contains slightly distorted planar BO_3 groups separated by Sr^{2+} ions. $\text{Sr}_2\text{B}_2\text{O}_5$ contains B_2O_5 groups, each of which is formed by two BO_3 triangles linked via common vertices. SrB_2O_4 was found to be polymorphic under high pressure. The crystal structure of SrB_2O_4 prepared under ambient pressure consists of 1D chains of corner-sharing BO_3 triangles,¹⁵ while that of the high-pressure phase consists of a fully connected 3D framework of corner-sharing BO_4 tetrahedra.¹⁶ SrB_4O_7 is also characterized by a 3D network of corner-sharing BO_4 tetrahedra. However, this network is different from that observed in the high-pressure phase of SrB_2O_4 . In an attempt to synthesize noncentrosymmetric compounds that are potentially applicable as NLO materials, Tang et al.¹⁸ have unexpectedly obtained single crystals of $\text{Sr}_2\text{B}_{16}\text{O}_{26}$. X-ray structural analysis established that this compound is a B_2O_3 -richest phase ($\text{B}_2\text{O}_3/\text{SrO} = 4$) in the $\text{SrO}-\text{B}_2\text{O}_3$ system and crystallizes in a totally new structure type (Pearson symbol mP176) which is unknown for the borates. So an investigation of the band structure may play a crucial role in understanding of the physical properties and predictions of this compound. First-principle band structure calculations have been successfully used to obtain fundamental parameters of semiconductors and dielectrics. The structural parameters and dynamical properties of crystals determine a wide range of microscopic and macroscopic features, i.e., diffraction, sound velocity, elastic constants, Raman and infrared absorption, inelastic neutron scattering, and specific heat, etc.

To the best of our knowledge, no comprehensive work, neither experimental data on the fundamental optical functions or first principles band structure calculations of the electronic features of strontium borate $\text{Sr}_2\text{B}_{16}\text{O}_{26}$, has appeared in the literature. This work is a natural continuation of the previous

* To whom correspondence should be addressed. Tel.: +420 777729583. Fax: +420-386 361231. E-mail: maalidph@yahoo.co.uk.

† South Bohemia University.

‡ Indian Institute of Technology Kanpur.

§ Technological University of Czestochowa.

|| Beijing University of Technology.

experimental work of Tang et al.¹⁸ A detailed depiction of the electronic and optical properties of $\text{Sr}_2\text{B}_{16}\text{O}_{26}$ using full potential method is timely and would bring us important insights in understanding the origin of the electronic band structure and densities of states. The earlier investigations of the borates have been performed within a framework of the norm-conserving pseudopotential methods¹⁹ which are suitable for the optical properties and may be not so good for the more deep corelike valence states. That is a reason for the choosing of the full potential linear augmented plane wave (FP-LAPW) calculations procedure. The present study is aimed toward calculations using the FP-LAPW method, which has proven to be one of the most accurate methods^{20,21} for the computation of the electronic structure of solids within a framework of density functional theory (DFT).

Section 2 is devoted to the experimental procedure. Theoretical calculations details are given in the section 3. Principal experimental results and their comparison with the theory are given in section 4.

2. Experimental Procedure

The title compound was synthesized by employing a conventional solid-state reaction method. All reagents were of analytical grade. For the preparation of $\text{Sr}_2\text{B}_{16}\text{O}_{26}$ crystals, a powder mixture of 0.437 g of Bi_2O_3 , 0.139 g of SrCO_3 , and 1.004 g of H_3BO_3 (the $\text{Bi}_2\text{O}_3/\text{SrO}/\text{B}_2\text{O}_3$ molar ratio = 3:3:26) was transferred to a small Au crucible. The sample was gradually heated to 735 °C, where it was kept for 2 weeks, then cooled to 500 °C at a rate of 5 °C/h, and followed by cooling to room temperature at a rate of 20 °C/h. The colorless, blocklike crystals of $\text{Sr}_2\text{B}_{16}\text{O}_{26}$ with dimensions up to $0.4 \times 0.4 \times 0.5$ mm³ were embedded in a borate matrix. Several small crystals were isolated mechanically from the reaction product and checked by energy-dispersive X-ray analyses in a scanning electron microscope, which showed the presence of strontium as the only heavy element. Although Bi did not enter the crystals, bismuth borate acted as a flux that is favorable for the crystal growth. A small single crystal was glued on a glass fiber and put on an automated Rigaku AFC7R four-circle diffractometer equipped with graphite-monochromatic Mo K α radiation ($\lambda = 0.71073$ Å). The data were collected at room temperature by using a $2\theta - \omega$ scan technique and corrected for Lorentz and polarization effects, and for absorption by empirical method based on ψ -scan data. The crystal structure was solved by a direct method and refined in the SHELX-97 system by full-matrix least-squares methods on F_0^2 . All atoms were refined anisotropically. The final cycle of refinement converged to R1/wR2 = 0.0395/0.0751 for 3724 observed reflections [$I \geq 2\sigma(I)$] and 397 variables. Details of crystal parameters as well as the atomic coordinates and the equivalent isotropic displacement parameters have been presented in our previous works,¹⁸ and theoretical calculations in this work are based on the model built from our measured atomic parameters.¹⁸

For the preparation of the single-phase polycrystalline sample of $\text{Sr}_2\text{B}_{16}\text{O}_{26}$, a stoichiometric mixture of SrCO_3 and H_3BO_3 was heated at 600 °C for 2 weeks with several intermediate remixings, and the resulting products were identified by powder X-ray analysis using the monochromatized Cu K α radiation of a Bruker D8 ADVANCE diffractometer. Figure 1a shows the observed X-ray diffraction (XRD) pattern together with that calculated from the single-crystal data for comparison. It is clear that the observed XRD pattern is in good agreement with the theoretical one, further confirming that our structural model is correct and the pure-phase sample of $\text{Sr}_2\text{B}_{16}\text{O}_{26}$ has been obtained.

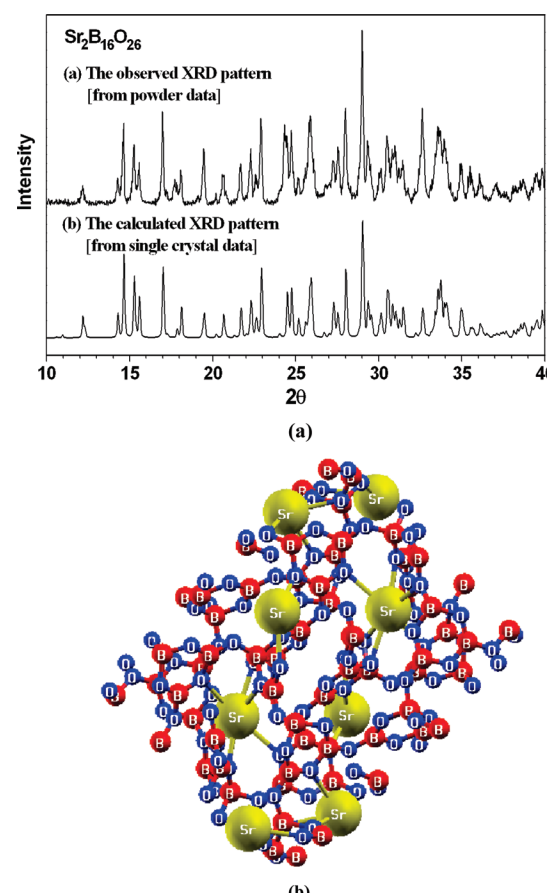


Figure 1. (a) Calculated and observed X-ray diffraction profiles. (b) Crystal structure.

The sample's surface was bombarded with X-rays, and the concomitant photoemitted electrons which exhibit discrete kinetic energies were measured. Those energies characterize the emitting atoms and their bonding states. We used high vacuum equal to 10^{-10} Torr. The high-energy resolution analyzer gave an opportunity to perform the photoemitted electrons analysis up to 0.12 eV. By minimizing the wave spread of the entering photoelectrons, the precision of energy determination was enhanced. Additionally, the spot size was decreased to 22 μm . This enabled us to analyze different parts of the surfaces. X-ray beams imparted precise energy to the photoelectrons and allowed us to extract chemical and bonding information. Using monochromatic X-rays precisely helped to remove satellites from the Al K X-ray line. This ensured the precise impartation of energy to photoelectrons.

3. Theoretical Calculation

The single-crystal X-ray structural analysis shows that the single crystal of $\text{Sr}_2\text{B}_{16}\text{O}_{26}$ crystallizes in the monoclinic space group $P2_1/c$ with $a = 8.408(1)$ Å, $b = 16.672(1)$ Å, $c = 13.901(2)$ Å, $\beta = 106.33(1)$ °, and $Z = 4$ (see Figure 1b). Its crystal structure consists of a 3D network of the complex borate anion $[\text{B}_{16}\text{O}_{20}\text{O}_{12/2}]^{4-}$, formed by 12 BO₃ triangles and four BO₄ tetrahedra, which can be viewed as three linked $[\text{B}_3\text{O}_3\text{O}_{4/2}]^-$ triborate groups bonded to one pentaborate $[\text{B}_5\text{O}_6\text{O}_{4/2}]^-$ group and two BO₃ triangles; this leads to a fundamental building block (FBB) with the shorthand notation 16: $\infty^3[3 \times (3: 2\Delta + T) + (5: 4\Delta + T) + 2\Delta]$. The 3D network affords interesting open channels running parallel to the crystallographic a and c axes, where Sr²⁺ cations reside.

We have performed calculations using all-electron FP-LAPW method to solve the Kohn–Sham DFT equations within the framework of the WIEN2K code.²² This is an implementation of the DFT²³ with different possible approximation for the exchange correlation (XC) potentials. The exchange correlation potential was calculated using the generalized gradient approximation (GGA)²⁴ as modified by Engel–Vosko.²⁵ The Engel–Vosko GGA formalism²⁵ optimizes the exchange correlation potential for band structure and optical properties calculations. It is well-known in the self-consistent band structure calculation within DFT, that both the local density approximation (LDA) and GGA approaches usually underestimate the energy gap's values.²⁶ This is mainly due to the fact that they are based on simple model assumptions which are not sufficiently flexible to accurately reproduce the exchange correlation energy and its charge space derivative. Engel and Vosko considered this shortcoming and constructed a new functional form of GGA²⁵ which is able to reproduce better exchange potential at the expense of less agreement in the exchange energy. This approach (EV-GGA) yields better band splitting compared to the GGA. For the electronic and optical properties we have applied the EV-GGA scheme.²⁵

To achieve energy eigenvalues convergence, the wave functions in the interstitial regions were expanded in plane waves with a cutoff $K_{\max} = 9/R_{\text{MT}}$, where R_{MT} denotes the smallest atomic sphere radius and K_{\max} gives the magnitude of the largest \mathbf{K} vector in the plane wave expansion. The muffin-tin radii were assumed to be 1.9, 1.05, and 1.25 atomic units (au) for Sr, B, and O, respectively. The valence wave functions inside the spheres were expanded up to $l_{\max} = 10$, while the charge density was Fourier expanded up to $G_{\max} = 14 \text{ au}^{-1}$. Self-consistency was achieved by use of 300 \mathbf{k} -points in the irreducible Brillouin zone (IBZ). The density of states and the optical properties are calculated using 500 \mathbf{k} -points of the IBZ. The self-consistent calculations are considered to be converged when the total energy of the system is stable within 10^{-5} Ry .

4. Results and Discussion

a. Band Structure, Density of States, and Electron Charge Density. The band structure and total density of states (DOS) along with the Sr-s/p/d, B-s/p, and O-s/p partial DOS are shown in Figures 2 and 3a–d. Our calculations show that the valence band maximum (VBM) and conduction band minimum (CBM) are located at Γ of the Brillouin zone (BZ), resulting in a direct energy gap of about 5.31 eV. The electronic structure of the upper valence band originates predominantly from the O-s/p, B-p, and Sr-s/p interactions. The electronic structure of the lower conduction band is dominated by the Sr-d, O-p, Sr-s/p, and B-s/p interactions. The existence of O-p states in the upper valence band and lower conduction band has significant effect on the energy band gap dispersion. Following Figure 3a–d, we can notice that the DOS can be divided into three principal spectral structures separated by gaps. The lowest groups in the energy around −16.0 to −15.0 eV originates mainly from O-s, Sr-p, and B-s/p states. The bands from −15.0 up to −5.5 eV are an admixture of O-p and B-s/p states with small admixture of O-s and Sr-s/p states. The third structure from Fermi energy and above originate from Sr-d, O-p, and B-s/p with small contributions of Sr-s/p and O-s states.

From PDOS one can see that there exists a strong hybridization between B-s and B-p states at around −15.0, −10.0, and +7.0 eV. In the energy region around −16.0 to −12 eV, O-s hybridizes with Sr-p and Sr-s strongly hybridizes with Sr-p states in the energy regions between E_F to 7.0 eV.

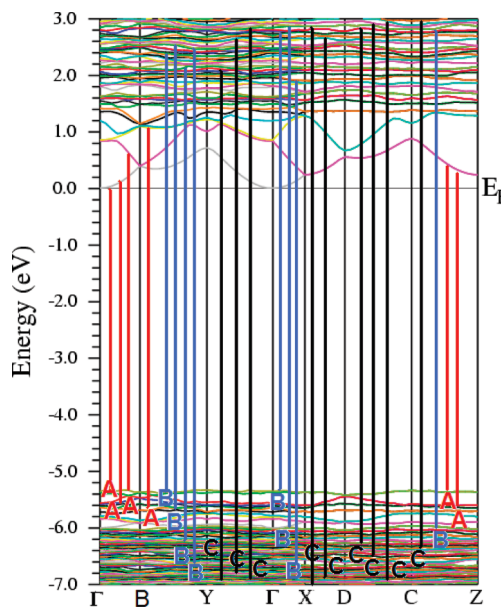


Figure 2. Calculated band structure along with the optical transitions.

We can elucidate the nature of chemical bonding from the total and partial DOS. We observe that the DOS, extending from −15.0 to −5.0 eV, is larger for O-p states (1.0 electrons/eV), B-p states (0.1 electrons/eV), Sr-p states (0.045 electrons/eV), and O-s states (0.03 electrons/eV) by comparing the total DOS with the angular momentum projected DOS of O-p, B-p, Sr-p, and O-s states, as shown in Figure 3a–d. These results show that some electrons from O-p, B-p, Sr-p, and O-s states are transferred into valence bands (VBs) and contribute in weak covalence interactions between O–O, B–B and Sr–Sr atoms, and the substantial covalence interactions between B and O, and Sr and O atoms.

In Figure 4, our experimental VB-XPS of the single crystal of $\text{Sr}_2\text{B}_{16}\text{O}_{26}$ is compared with results of our full potential linear augmented plane wave method using the Engel–Vosko GGA exchange correlation functional. The calculated TDOS spectrum reproduces the general structure of the measured XPS valence band correctly, probably due to the better representation of the wave functions in the FP-LAPW method. The valence band density of states data were analyzed in the energy range in which the experiment was performed (−16.0 to −5.0 eV). We note a reasonable agreement in the matter of the general behavior and position of the peaks that is attributed to the use of the full potential method. However, the magnitude of theoretical DOS is significantly different from the experimental one. We would like to mention that the difference between the magnitudes of the experimental and the theoretical curves can be made smaller if we choose a larger broadening in our theoretical calculations. In the present calculation the broadening is around 0.003 eV.

Turning now to the bonding properties, the bonding nature of the solids can be described accurately by using electronic density plots,^{27,28} that have been calculated in the context of first-principles approach. The charge density in our calculation is derived from a highly converged wave function; hence, the result is very reliable, and it can then be used to study the bonding nature of the solid. To visualize the nature of the bonding character and to explain the charge-transfer and bonding properties, we calculated the total valence charge density; we present in Figure 5a,b, the total valence charge densities in the (1 1 0) plane. There is a strong covalent bond existing between the Sr and O, and B and O atoms. The strength of the chemical

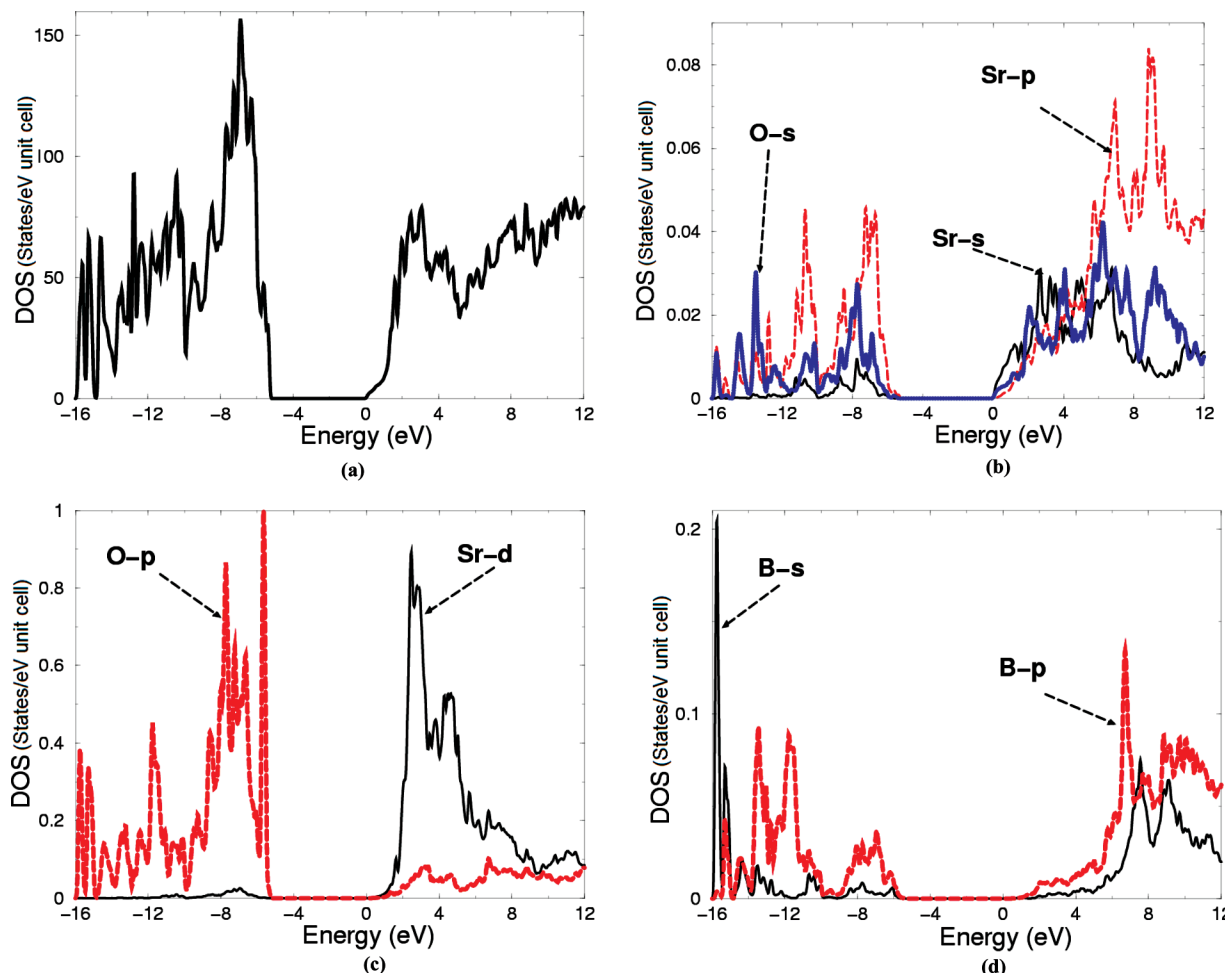


Figure 3. (a) Total density of states (states/eV unit cell) along with the partial density of states; (b) Sr-s/p and O-s; (c) Sr-d and O-p; (d) B-s/p.

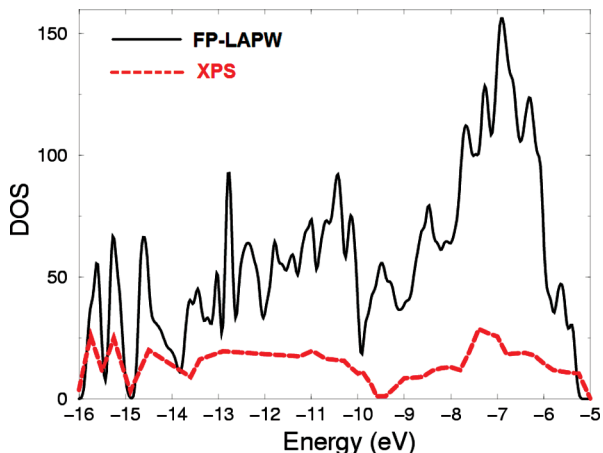


Figure 4. Total density of states (states/eV unit cell) using FP-LAPW method in comparison with the measured total density of states using XPS technique for the valence band.

bonds of Sr–Sr, O–O, and B–B bonds are found to be weaker than the Sr–O and B–O bonds. The calculated charge densities also allow analysis of the nature of the bonds in this compound according to a classical chemical concept. This concept is very useful to classify compounds into different categories with different chemical and physical properties.

b. First-Order (Linear) Optical Susceptibilities. Strontium borate $\text{Sr}_2\text{B}_{16}\text{O}_{26}$ crystallizes in the monoclinic space group $P2_1/c$ with four formula units per unit cell. This symmetry group has

two dominant components of the dielectric tensor. The dielectric functions are $\varepsilon_{\perp}^{\text{xx}}(\omega)$ and $\varepsilon_{\parallel}^{\text{zz}}(\omega)$ corresponding to the electric field direction parallel and perpendicular to the crystallographic c axis. The calculation of $\varepsilon_2(\omega)$ requires the precise values of energy eigenvalues and electron wave functions. These are natural outputs of a band structure calculation. In general the optical properties of matter can be described by means of the transverse dielectric function $\varepsilon(\omega)$. Generally there are two contributions to $\varepsilon(\omega)$, namely, due to intraband and interband transitions. The contribution due to intraband transitions is crucial only for metals. The interband transitions of the dielectric function $\varepsilon(\omega)$ can be split into direct and indirect transitions. We neglect the indirect interband transitions involving scattering of phonons, assuming that they give a small contribution to $\varepsilon(\omega)$ for the case of the borates.²⁹ To calculate the direct interband contributions to the imaginary part of the dielectric function $\varepsilon_2(\omega)$, it is necessary to perform summation over the BZ structure for all possible transitions from the occupied to the unoccupied states. Taking the appropriate transition matrix elements into account, we calculated the imaginary part of the dielectric functions $\varepsilon_2(\omega)$ using the expressions given in Refs. 30 and 31.

Figure 6a depicts the variation of the imaginary part of the frequency-dependent electronic dielectric function $\varepsilon_2(\omega)$. The spectral broadening is taken to be 0.04 eV. The calculated imaginary part $\varepsilon_2(\omega)$ can be used to describe the transitions between the occupied and unoccupied bands. Following the $\varepsilon_2(\omega)$ spectra one can conclude that the principal peaks are

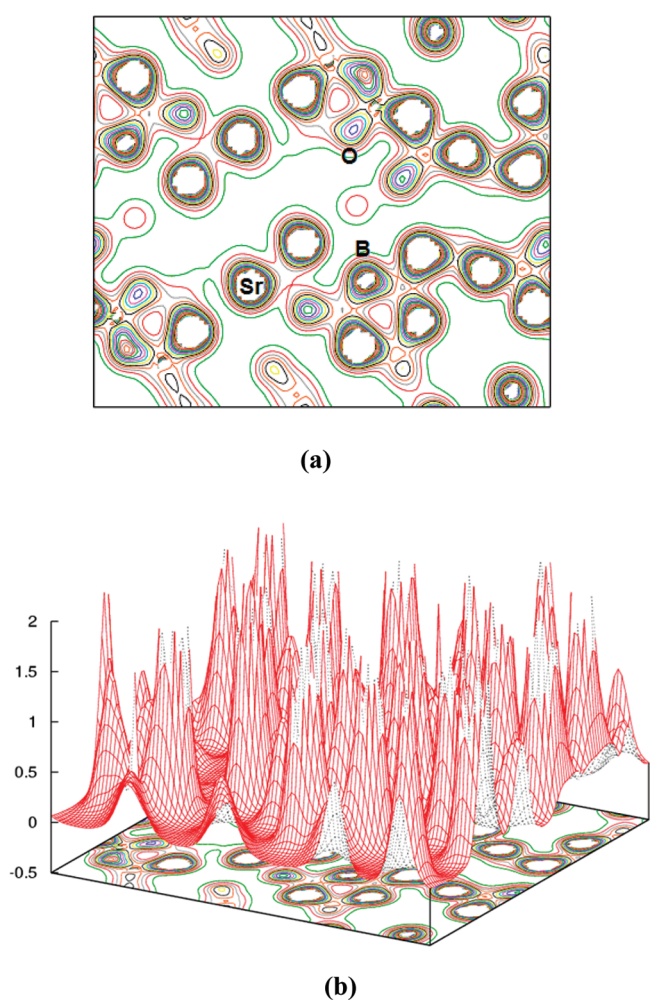


Figure 5. (a) Total valence charge densities in the (1 1 0) plane (2D). (b) Total valence charge densities in the (1 1 0) plane (3D).

situated at energies around 9.0 eV for $\varepsilon_2^{\text{xx}}(\omega)$ and 10.5 for $\varepsilon_2^{\text{yy}}(\omega)$. We should emphasize that there is a weak anisotropy between $\varepsilon_2^{\text{xy}}(\omega)$ and $\varepsilon_2^{\text{zz}}(\omega)$. The peaks in the optical response are caused by the allowed electric-dipole transitions between the valence and conduction bands. To identify these structures, we should consider the magnitude of the optical dipole matrix elements. The observed structures would correspond to those transitions which have larger optical matrix dipole transition elements. It would be worthwhile to attempt to identify the interband transitions that are responsible for the spectral features in $\varepsilon_2^{\text{xy}}(\omega)$ and $\varepsilon_2^{\text{zz}}(\omega)$ using our calculated density of states and band structure. The optical transitions occur between the occupied Sr-s/p, O-s/p, and B-s/p states and the unoccupied Sr-s/p/d, O-s/p, and B-s/p states. Figure 2 shows the optical transitions which are responsible for the spectral structures in $\varepsilon_2^{\text{xy}}(\omega)$ and $\varepsilon_2^{\text{zz}}(\omega)$. For simplicity we have labeled the transitions in Figure 2, as A–C. Transitions A are responsible for the structures in $\varepsilon_2^{\text{xy}}(\omega)$ and $\varepsilon_2^{\text{zz}}(\omega)$ for energies up to 6.0 eV, transitions B are responsible for the structures in the energy range of 6.0–9.0 eV, and transitions C are responsible for the spectral structures between 9.0 eV and above.

From the spectral dependences of imaginary parts of the dielectric function $\varepsilon_2^{\text{xy}}(\omega)$ and $\varepsilon_2^{\text{zz}}(\omega)$ the real parts $\varepsilon_1^{\text{xy}}(\omega)$ and $\varepsilon_1^{\text{zz}}(\omega)$ can be calculated using Kramers–Kronig relations.³² Our calculated real parts are shown in Figure 6b. Again it shows a weak anisotropy between $\varepsilon_1^{\text{xy}}(\omega)$ and $\varepsilon_1^{\text{zz}}(\omega)$. The static dielectric constant $\varepsilon_1(0)$ is given by the low-energy limit of $\varepsilon_1(\omega)$. Note

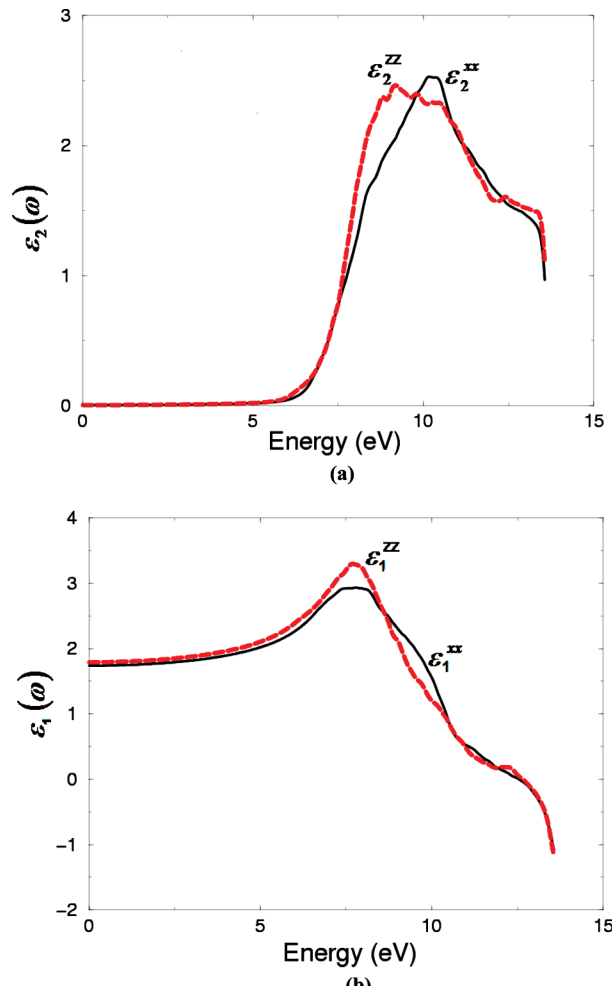


Figure 6. (a) Calculated dispersions of imaginary parts $\varepsilon_2^{\text{xy}}(\omega)$ (black solid curve) and $\varepsilon_2^{\text{zz}}(\omega)$ (red dashed curve) spectra. (b) Calculated dispersions of real parts $\varepsilon_1^{\text{xy}}(\omega)$ (black solid curve) and $\varepsilon_1^{\text{zz}}(\omega)$ (red dashed curve).

that we do not include phonon contributions to the dielectric screening. $\varepsilon_1(0)$ corresponds to the static optical dielectric constant (ε_∞). The calculated value of $\varepsilon_1^{\text{xy}}(0)$ is 1.74 and 1.75 for $\varepsilon_1^{\text{zz}}(0)$. The uniaxial anisotropy [$\delta\varepsilon = (\varepsilon_0^{\text{zz}} - \varepsilon_0^{\text{xy}})/\varepsilon_0^{\text{tot}}$] is 0.00847, indicating a weak anisotropy³³ of the dielectric function.

For more detailed information about the optical properties of the investigated crystal we have calculated the frequency-dependent reflectivity $R(\omega)$, refractive index $n(\omega)$, extinction coefficient $k(\omega)$, optical conductivity $\sigma(\omega)$, and loss function. Figure 7a shows the calculated reflectivity spectra. We notice that a reflectivity maximum around 8.0 eV arises from interband transitions. A reflectivity minimum at energies ranging from about 12.5 eV confirms an occurrence of collective plasma resonance. The depth of the plasma minimum is determined by the imaginary part of the dielectric function at the plasma resonance and is representative of the degree of overlap between the interband absorption regions. We should note that at high energies (at around 13.0 eV) this crystal shows rapidly increasing reflectivity. The calculated refractive index $n(\omega)$ is shown in Figure 7b. Generally a compound which shows considerable anisotropy in the linear optical susceptibilities favors an important quantity in second harmonic generation (SHG) and optical parametric oscillator (OPO) due to better fulfilling of phase matching conditions, determined by birefringence. The birefringence is the difference between the extraordinary and

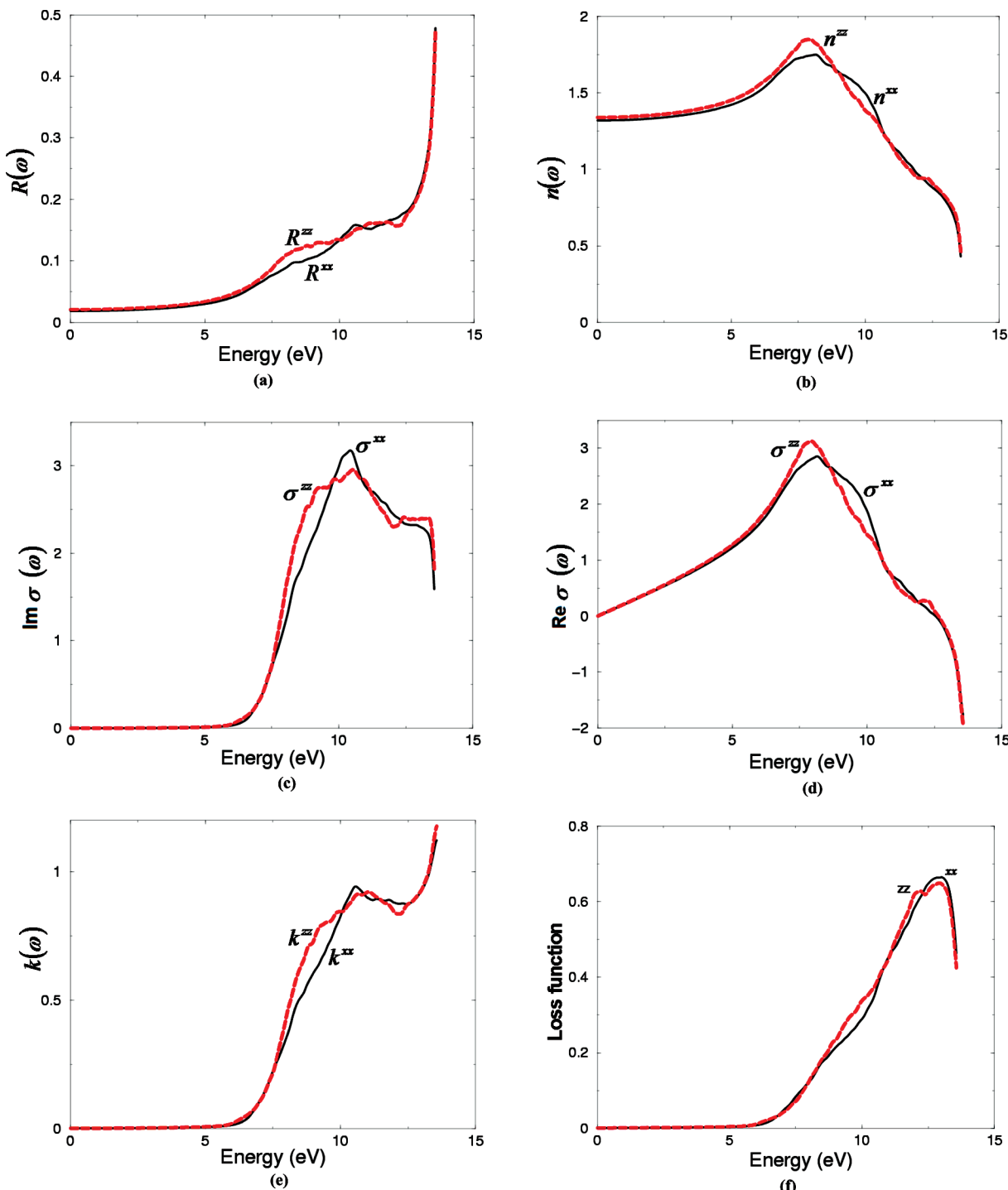


Figure 7. (a) Calculated $R^{xx}(\omega)$ (black solid curve) and $R^{zz}(\omega)$ (red dashed curve) spectrum. (b) Calculated refractive index $n^{xx}(\omega)$ (black solid curve) and $n^{zz}(\omega)$ (red dashed curve) spectrum. (c) Calculate Calculated imaginary part of $\sigma^{xx}(\omega)$ (black solid curve) and $\sigma^{zz}(\omega)$ (red dashed curve) spectrum. (d) Calculated real part of $\sigma^{xx}(\omega)$ (black solid curve) and $\sigma^{zz}(\omega)$ (red dashed curve) spectrum. (e) Calculated extinction coefficient $k^{xx}(\omega)$ (balck solid curve) and $k^{zz}(\omega)$ (red dashed curve) spectrum. (f) Calculated loss function of $L^{xx}(\omega)$ (back solid curve) and $L^{zz}(\omega)$ (red dashed curve) spectrum.

ordinary refraction indices, $\Delta n = n_e - n_o$, where n_e is the index of refraction for an electric field oriented along the c axis and n_o is the index of refraction for an electric field perpendicular to the c axis. Since this crystal shows very weak anisotropy, as a consequence it possesses negligible birefringence $\Delta n(\omega)$. Birefringence is important only in the nonabsorbing region, which is below the energy gap. Thus, this crystal is expected not to be a phase matching material. The calculated optical conductivity $\sigma(\omega)$ components are shown in Figure 7c,d. It also shows a weak anisotropy between $\sigma^{xx}(\omega)$ and $\sigma^{zz}(\omega)$. The optical

conductivity (OC) $\sigma(\omega)$ is related to the dielectric function $\epsilon(\omega)$ as $\epsilon(\omega) = 1 + (4\pi i\sigma(\omega)/\omega)$. The peaks in the optical conductivity spectra are determined by the electric-dipole transitions between the occupied states to the unoccupied states. As there are no experimental or theoretical results for the optical properties available for these compounds, we hope that our work will stimulate more works. Also we have calculated $k(\omega)$ as shown in Figure 7e; again it shows weak anisotropy between the two components. In Figure 7f, we present the electron energy loss $L(\omega)$ spectra. In the energy loss spectra we do not see any

distinct maxima at the low-energy range. With the increase of the energy, $\varepsilon_2(\omega)$ has a slow decrease. However, at high energy, $\varepsilon_2(\omega)$ is smaller and thus the amplitude of the energy loss becomes large. The main peak in the energy loss function, which defines the screened plasma frequency ω_p , is located at 12.5 eV. These main peaks correspond to the abrupt reduction of the reflectivity spectrum $R(\omega)$ and to the zero crossing of $\varepsilon_1(\omega)$.

5. Conclusions

Experimental and theoretical work has been performed on a single crystal of strontium borate $\text{Sr}_2\text{B}_{16}\text{O}_{26}$. The experimental work was done with XRD and XPS and compared with the results of the first principles calculations using the full potential method. The total density of states (DOS) along with the Sr-s/p/d, B-s/p, and O-s/p partial DOS were calculated. Our calculations show that the VBM and CBM are located at Γ , resulting in a direct energy gap of about 5.31 eV. The experimental VB-XPS was compared with the VB-FPLAPW. Reasonable agreement was found with respect to the band energy dispersion and spectral positions of the principle peaks. To visualize the nature of the bonding and to explain the charge transfer, we have calculated the total valence charge density in the (1 1 0) plane. The strength of the chemical bonds Sr–Sr, O–O, and B–B bonds are found to be weaker than the Sr–O and B–O bonds. The frequency-dependent dielectric function, reflectivity, conductivity, extinction coefficient, refractive index, and the loss function were calculated. From the calculated optical properties we found that the uniaxial anisotropy is about 0.00847, indicating a weak anisotropy of the dielectric function; as a consequence the investigated crystal possesses negligible birefringence $\Delta n(\omega)$.

Acknowledgment. For A.H.R. this work was supported from the institutional research concept of the Institute of Physical Biology, UFB (Grant No. MSM6007665808). For X.C. the work was supported from the Funding Project for Academic Human Resources Development in Institutions of Higher Learning under the Jurisdiction of Beijing Municipality, and the National Natural Science Foundation of China (Grant No. 20871012).

References and Notes

- (1) Liebertz, J. *Z. Kristallogr.* **1982**, *158*, 319. Liebertz, J.; Stahr, S. *Z. Kristallogr.* **1983**, *165*, 195.
- (2) Weizhuo, Z.; Huicong, H.; Zhiping, L.; Thiande, Z.; Sukun, H.; Dingyuan, T.; Qinglan, Z. *Sci. China, Ser. B* **1995**, *38*, 2.
- (3) Becker, P.; Liebertz, J.; Bohaty, L. *J. Cryst. Growth* **1999**, *203*, 149.
- (4) Kaminskii, A. A.; Becker, P.; Bohaty, L.; Ueda, K.; Takaichi, K.; Hanuza, J.; Maczka, M.; Eichler, H. J.; Gad, M. A. *Opt. Commun.* **2002**, *206*, 179. Burianek, M.; Held, P.; Muhlberg, M. *Cryst. Res. Technol.* **2002**, *37*, 179.
- (5) Burianek, M.; Held, P.; Muhlberg, M. *Cryst. Res. Technol.* **2002**, *37*, 785.
- (6) Filatov, S.; Shepelev, Y.; Bubnova, R.; Sennova, N.; Egorysheva, A. V.; Kargin, Y. F. *J. Solid State Chem.* **2004**, *177*, 515.
- (7) Lin, Z.; Wang, Z.; Chen, C.; Lee, M. H. *J. Appl. Phys.* **2001**, *90*, 5585.
- (8) Xue, D.; Betzler, K.; Hesse, H.; Lammers, D. *Solid State Commun.* **2000**, *21*, 114.
- (9) Becker, P. *Adv. Mater.* **1998**, *10*, 979.
- (10) Grice, J. D.; Burns, P. C.; Hawthorne, F. C. *Can. Mineral.* **1999**, *37*, 731.
- (11) Chen, C. T.; Wu, B.; Jiang, A.; You, G. *Sci. China, Ser. B* **1985**, *18*, 235.
- (12) Oseledchik, Yu. S.; Prosvirnin, A. L.; Pisarevskiy, A. I.; Starshenko, V. V.; Osadchuk, V. V.; Belokrys, S. P.; Svitanko, N. V.; Korol, A. S.; Krikunov, S. A.; Selevich, A. F. *Opt. Mater.* **1995**, *4*, 669.
- (13) Wei, Z. F.; Chen, X. L.; Wang, F. M.; Li, W. C.; He, M.; Zhang, Y. *J. Alloys Compd.* **2001**, *327*, 10.
- (14) Lin, Q.-S.; Cheng, W.-D.; Chen, J.-T.; Huang, J.-S. *J. Solid State Chem.* **1999**, *144*, 30.
- (15) Kim, J.-B.; Lee, K.-S.; Suh, I.-H.; Lee, J.-H.; Park, J.-R.; Shin, Y.-H. *Acta Crystallogr., C* **1996**, *52*, 498.
- (16) Ross, N. L.; Angel, R. J. *J. Solid State Chem.* **1991**, *90*, 27.
- (17) Perloff, A.; Block, S. *Acta Crystallogr.* **1966**, *327*, 274.
- (18) Zhi-Hua, Tang; Xuean, Chen; Ming, Li. *Solid State Sci.* **2008**, *10*, 894.
- (19) Smok, P.; Kityk, I. V.; Plucinski, K. J.; Berdowski, J. *Phys. Rev. B* **2002**, *65*, 205103.
- (20) Shiwu, Gao *Comput. Phys. Commun.* **2003**, *153*, 190.
- (21) Schwarz, K. *J. Solid State Chem.* **2003**, *176*, 319–328.
- (22) Blaha, P.; Schwarz, K.; Madsen, G. K. H.; Kvasnicka, D.; Luitz, J. In *WIEN 2K, An Augmented Plane Wave + Local Orbitals Program for Calculating Crystal Properties*; Schwarz, K., Ed.; Technische Universität, Wien, Austria, 2001; ISBN 3-9501031-1-2.
- (23) Hohenberg, P.; Kohn, W. *Phys. Rev. B* **1964**, *136*, 864.
- (24) Perdew, J. P.; Burke, S.; Ernzerhof, M. *Phys. Rev. Lett.* **1996**, *77*, 3865.
- (25) Engel, E.; Vosko, S. H. *Phys. Rev. B* **1993**, *47*, 13164.
- (26) Dufek, P.; Blaha, P.; Schwarz, K. *Phys. Rev. B* **1994**, *50*, 7279.
- (27) Hoffman, R. *Rev. Mod. Phys.* **1988**, *60*, 801.
- (28) Gellatt, C. D.; Williams, A. R.; Moruzzi, V. L. *Phys. Rev. B* **2005**, *72*, 1983.
- (29) Smith, N. V. *Phys. Rev. B* **1971**, *3*, 1862.
- (30) Hufner, S.; Claessen, R.; Reinert, F.; Straub, Th.; Strocov, V. N.; Steiner, P. *J. Electron Spectrosc. Relat. Phenom.* **1999**, *191*, 100. Ahuja, R.; Auluck, S.; Johansson, B.; Khan, M. A. *Phys. Rev. B* **1994**, *50*, 2128.
- (31) Ali Hussain, Reshak; Kityk, I. V.; Auluck, F. *J. Chem. Phys.* **2008**, *129*, 074706.
- (32) Tributsch, H. *Z. Naturforsch. A* **1977**, *32A*, 972.
- (33) Reshak, A. H. *Ph.D. Thesis*, Indian Institute of Technology—Roorkee, India, 2005.

JP903170P